The Astrophysical Journal, 692:1271–1286, 2009 February 20 doi:10.1088/0004-637X/692/2/1271

THREE-DIMENSIONAL STRUCTURE AND ENERGY BALANCE OF A CORONAL MASS EJECTION

J.-Y. Lee[1,2,3], J. C. Raymond[2], Y.-K. Ko[2], and K.-S. Kim[1]
[1] Department of Astronomy and Space Science, Kyung Hee University, Yongin, Gyeonggi, 446-701, Korea
[2] Harvard-Smithsonian Center for Astrophysics, Cambridge, MA 02138, USA
[3] NorthWest Research Associates, CoRA Division, Boulder, CO 80301, USA
Received 2007 October 31; accepted 2008 October 26; published 2009 February 24

ABSTRACT

The Ultraviolet Coronagraph Spectrometer (UVCS) observed Doppler-shifted material of a partial halo coronal mass ejection (CME) on 2001 December 13. The observed ratio of [O v]/O v] is a reliable density diagnostic important for assessing the state of the plasma. Earlier UVCS observations of CMEs found evidence that the ejected plasma is heated long after the eruption. We have investigated the heating rates, which represent a significant fraction of the CME energy budget. The parameterized heating and radiative and adiabatic cooling have been used to evaluate the temperature evolution of the CME material with a time-dependent ionization state model. The functional form of a flux-rope model for interplanetary magnetic clouds was also used to parameterize the heating. We find that continuous heating is required to match the UVCS observations. To match the O vi bright knots, a higher heating rate is required such that the heating energy is greater than the kinetic energy. The temperatures for the bright knots in Lyα and C iii emission indicate that smaller heating rates are required for those regions. In the context of the flux-rope model, about 75% of the magnetic energy must go into heat in order to match the O vi observations. We derive tighter constraints on the heating than earlier analyses, and we show that thermal conduction with the *Spitzer* conductivity is not sufficient to account for the heating at large heights.

Key words: Sun: activity – Sun: corona – Sun: coronal mass ejections (CMEs) – Sun: UV radiation

Online-only material: mpeg animation

1. INTRODUCTION

The Ultraviolet Coronagraph Spectrometer (UVCS) on board the *Solar and Heliospheric Observatory* (*SOHO*) provides unique spectroscopic diagnostics of coronal mass ejection (CME) material through both Doppler shifts and line intensities (Raymond 2002). For CME studies, major questions are the three-dimensional structure and the energy budget of the ejected CME plasma. UVCS observations contribute to the understanding of these two major problems. The temperature evolution and energy balance during the ejection of CME have been studied by several authors (Akmal et al. 2001; Kumar & Rust 1996; Emslie et al. 2004; Vourlidas et al. 2000; Subramanian & Vourlidas 2007). Many studies of CME three-dimensional structure have been based on the two-dimensional projection of the three-dimensional structure on the plane of the sky and focused on efforts to overcome that loss of information (see Burkepile et al. 2004 and references therein). In this paper, we present the three-dimensional structure, heating, and energy balances for a CME observed on 2001 December 13.

The kinetic properties of CMEs from measurements of white light coronal observations have been determined, but suffer from the inaccuracies due to projection effects (Burkepile et al. 2004). Those make it difficult to study the three-dimensional structure. To overcome the projection effect, several geometrical assumptions such as the cone model (Zhao et al. 2002; Zie et al. 2004; Yeh et al. 2005), ice-cream cone model (Fisher & Munro 1984; Xue et al. 2005), and the time difference between the appearances of the halo at two opposite position angles (Michalek et al. 2003) have been applied to evaluate CME properties. The images reconstructed through polarization analysis indicate that CME is a bubble-like structure rather than an expanding loop arcade structure (Crifo et al. 1983; Moran & Davila 2004; Dere et al. 2006). Howard et al. (2007) used Solar Mass Ejection Imager (SMEI) data with the assumption of purely radial expansion from the eruption site to estimate the position of the ejecta in three dimensions. The three-dimensional structure reconstructed with UV emission lines observed by UVCS shows a ribbon-like structure in one event (Ciaravella et al. 2003) and a halo CME structure in the view from the solar west in another (Lee et al. 2006). The flux-rope model (Krall & St. Cyr 2006) compared statistically with CME observed by the *Solar Maximum Mission* (*SMM*) shows that the morphology of the CME is hollow (Krall 2007). The *Solar Terrestrial Relations Observatory* (*STEREO*) was launched on 2006 October 25, and two spacecraft trailing and leading Earth will provide future studies of the three-dimensional structure of CMEs (Kaiser 2005).

The line-of-sight velocity component observed by UVCS makes it possible to estimate the angle with the plane of the sky. For evaluating the required heating for the UVCS observations, this angle is used to estimate the radial velocities of the ejected plasma, and the column density from Large Angle and Spectrometric Coronagraph (LASCO) measurements. The angles with the plane of the sky have been evaluated for the 22 halo and partial halo CME cores observed by UVCS to estimate projection effects (Ciaravella et al. 2006).

The energy partitions for flare–CME events show that the CME has the dominant component of the released energy, and that it contains a substantial fraction of the available magnetic energy (Emslie et al. 2005). Studies of flux-rope CME kinetic energies also show that internal magnetic energy is a viable source of CME energy (Subramanian & Vourlidas 2007; Vourlidas et al. 2000). Earlier UVCS observations of CME found evidence that the ejected plasma is heated long after the eruption (Akmal et al. 2001; Ciaravella et al. 2001), and that the total heat going into the ejected plasma is comparable to the kinetic energy. Other studies based on the thermal energy evolution

of interplanetary coronal mass ejections (ICMEs) (Liu et al. 2006), emission in the EUV bands of the Extreme Ultraviolet Imaging Telescope (EIT) (Filippov & Koutchmy 2002), and the ionization states measured in ICMEs (Rakowski et al. 2007) also found that CME plasma is strongly heated even after it leaves the solar surface.

In this paper, we find the heating by a procedure similar to that of Akmal et al. (2001). We first generate a large grid of models with different initial conditions and forms of the heating function. Then, for individual knots observed by UVCS, we select all the models that match the observed spectra, and the range of heat inputs for those models is the range of heating allowed.

We find that continuous heating is required to match the UVCS observations. The temperature evolution shows a rapid decrease at lower heights and earlier stages, and then heating is required to increase the temperature to match the observations. To match the O VI bright knots, a higher heating rate is required such that the heating energy is greater than the kinetic energy. The temperatures for the O VI, Lyα, and C III emission indicate that different heating rates are required for knots that are bright in those lines. The required heating rates are much larger than wave heating rates for the quiet Sun, and they appear to be larger than predicted by thermal conduction. Magnetic heating should occur as the expanding magnetic flux rope dissipates energy to reach the simple configuration seen in interplanetary CMEs. The flux-rope model of Kumar & Rust (1996) predicts that somewhat more energy goes into heat than into kinetic energy. Our results for the knots bright in O VI are compatible with that prediction, while the heating rates for the knots bright in Lyα are smaller.

In Section 2 we describe UVCS, LASCO, EIT, and *Transition Region and Coronal Explorer* (*TRACE*) observations. In Section 3 we explain the expansion model for reconstructing the three-dimensional structure from a time sequence of long-slit spectra and show the three-dimensional structure of O VI, Lyα, and C III emissions observed by UVCS. In Section 4 we describe the observational constraints and the heating model. In Section 5, the results are presented in terms of the temperature evolution, heating energy, and energy balances. In Section 6 we discuss our results and compare the heating rates with those expected for thermal conduction. In Section 7 we summarize our studies.

2. OBSERVATIONS

UVCS (Kohl et al. 1995) obtains spectra of the solar corona inside an instantaneous field of view (FOV) given by the 40′ long spectrometer entrance slits and the slit width (21″ in this observation), which can be placed between 1.5 and 10 $R_\odot$. The UVCS slit was pointed above NOAA 9973 (N16 E09 at 14:20 UT on 2001 December 13) at a position angle P.A. = 349° at 2.4 $R_\odot$. The P.A. and height are the values at the point along the slit that is closest to the Sun center, which is 5/9 of the way from the east edge of the slit. The series of 300 s exposures separated by about 30 s readout time began many hours before the event and lasted until 19:16 UT at the same position. The data were obtained with a spatial binning of 6 pixels (42″) and a spectral binning of 1 pixel, 0.0993 Å and 0.0915 Å for primary and redundant wavelengths, respectively.

Figure 1 shows the composite image of EIT 195, UVCS, and LASCO C2 observations. A bright flare was observed in the EIT 195 Å band beginning at 14:24 UT, and the peak intensity was seen at 14:36 UT in the 12 min cadence images. In this event, *TRACE* observed this active region in the UV continuum

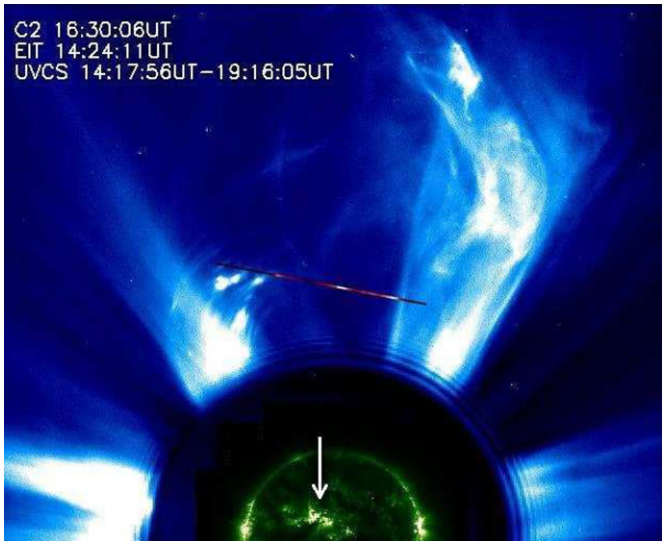

Figure 1. Composite image of EIT, UVCS and LASCO C2. The UVCS slit image shows the intensity distribution of the O VI line summed over exposures from 14:17:56 UT to 19:16:05 UT at 2.4 $R_\odot$ and P.A. = 349°. The arrow indicates the active region where the bright flare was observed.

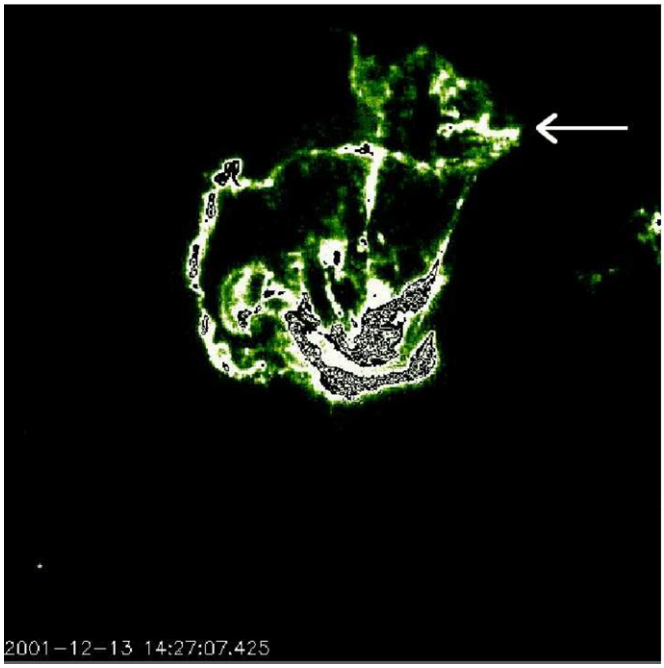

Figure 2. *TRACE* 1600 Å at 14:27:07 UT. The arrow indicates the filament eruption. The lower part of the active region was seen as dark due to a saturation.

(1600 Å and 1700 Å) and C IV 1550 Å. A filament eruption was observed in the UV continuum, 1600 Å around 14:20 UT (Figure 2). The leading edge of the CME first appeared in the LASCO C2 FOV at 14:54 UT, and in the C3 FOV at 16:18 UT. The *Geostationary Operational Environmental Satellite* (*GOES*) X6.2 class flare began at 14:20 UT, peaked at 14:30 UT, and lasted until 14:35 UT. Figure 3 shows the observation time of each instrument. EIT observed this active region with 12 min cadence. LASCO C2 and C3 obtain images with 24 min cadence, however the C2 and C3 data were not available from 14:54 UT–16:30 UT and 14:42 UT–16:18 UT during the CME expansion, respectively. At 14:54 UT, C2 observed the leading

Table 1
Blobs Observed by UVCS

Blob No.	UT	P.A.	Observed Lines
A	14:56:19	361°–366°	O VI, Lyα, C III, C II λ1036.34, C II λ1037.02, N III λ991.58
B.1	15:01:47	363°–364°	O VI, Lyα, C III, C II λ1036.34, C II λ1037.02, N III λ991.58
B.2		360°–361°	O VI, O V], Lyα, C II λ1037.02, N III λ991.58
B.3		350°–352°	O VI, O V], Lyα, C III, C II λ1036.34, C II λ1037.02, N III λ991.58
C.1	15:07:18	357°–358°	O VI, C III
C.2		350°–352°	O VI, O V], Lyα, C III, N III λ 989.90, N III λ991.58
C.3		347°	O VI, O V], [O V], Lyα, C III, C II λ1037.02, N III λ991.58
C.4		346°	O VI, O V], [O V], Lyα, C III, C II λ1037.02, N III λ991.58
C.5		345°	O VI, O V], [O V], Lyα, C III, C II λ1037.02, N III λ991.58
C.6		344°	O VI, O V], [O V], Lyα, C III, C II λ1037.02, N III λ991.58
D.1	15:12:48	347°	O VI, O V], Lyα, C III, N III λ991.58
D.2		346°	O VI, O V], [O V], Lyα, C III, C II λ1036.34, C II λ1037.02, N III λ991.58
D.3		345°	O VI, O V], [O V], Lyα, C III, C II λ1036.34, C II λ1037.02, N III λ991.58
D.4		344°	O VI, O V], [O V], Lyα, C III, N III λ991.58

edge of this event and then at the next observation, the CME has passed beyond the FOV of C2.

From 14:56 UT, UVCS observed Doppler-shifted material in the O VI 1032 Å, Lyα 1216 Å and C III 977 Å lines. Also the faint spectral lines O V] 1218.35 Å [O V] 1213.9 Å, N III 989.90 Å, N III 991.58 Å, C II 1036.34 Å, and C II 1037.02 Å were observed in several exposures. It is especially important that the observed O V] ($2s^2 {}^1S_0$–$2s2p^3 {}^1P_1$) intercombination line (violating the selection rule $\triangle S = 0$, notation: right square bracket, O V]) at 1218.35 Å and the [O V] ($2s^2 {}^1S_0$–$2s2p^3 {}^3P_2$) forbidden line (notation: square brackets, [O V]) at 1213.9 Å can be used to determine the plasma density (see Section 4.2.1). Because the Einstein A value of the forbidden line is 0.022 s^{-1}, the line is quenched at densities above about 10^6 cm^{-3} as shown in Figure 9 of Akmal et al. (2001). To investigate the heating rates, we analyzed the spectral lines for the 14 blobs observed in four exposures (refer to Table 1). Figure 4 shows the UVCS observations of O VI (each left panel) and Lyα, O V], [O V], N III (each middle panel), and C III (each right panel) from 14:56 UT to 15:12 UT. The Lyα and O V lines are observed in the redundant wavelength with the N III line in the primary wavelength. The positions along the slit of the 14 blobs are marked at the right axis of the middle panel with white bars. The intensities and line-of-sight velocities (V_{LOS}) of each blob are presented in Table 2 (O VI and O V) and Table 3 (Lyα, C III, C II, N III). For instance, in the case of blob A at the first detection of the CME at 14:56 UT, we selected the Doppler-shifted O VI emission with −0.98 Å and −1.68 Å (evaluated by two Gaussian fits) indicating line-of-sight velocities of −286 km s^{-1} and −459 km s^{-1}, respectively, at P.A. = 361°–366°. In the exposure at 15:01 UT, we selected three blobs (B.1, B.2, and B.3) and those are also marked on the left panel of Figure 4. The C III emission of blobs A and B was detected at the edge of the observed wavelength range in this data panel. In the case of region C observed at 15:07 UT, we selected six blobs, one detected only in O VI and C III (C.1), one detected in the bright emission of Lyα but relatively faint emission of O VI (C.2), and others detected in the emission of the forbidden [O V] λ1213.9 line (C.3–C.6). In the 15:12 UT observations, we selected four blobs (D.1–D.4) detected also in the emission of [O V]. The line intensities for most of blobs were evaluated by fitting two Gaussians to the line profile.

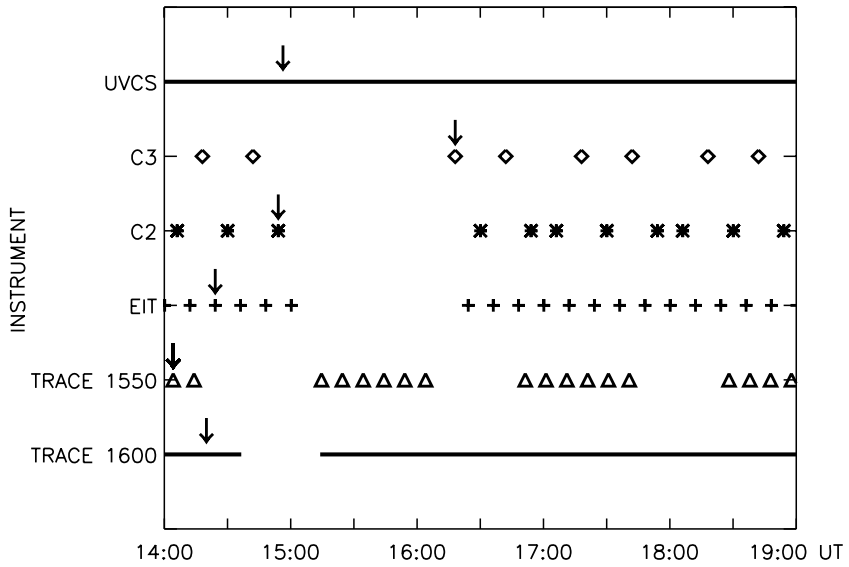

Figure 3. Observation time of each instrument. The arrows represent the first detection of this event at each instrument. In the *TRACE* 1550 Å observation, the bright emission had already started at 14:04 UT.

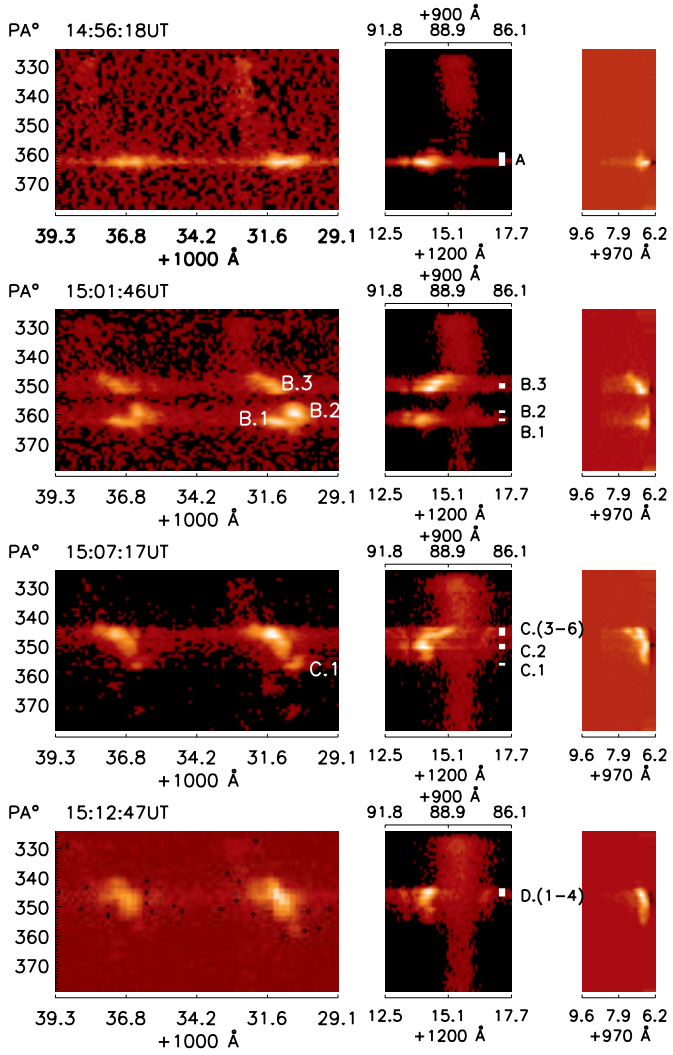

Figure 4. UVCS observations of the 2001 December 13 CME. The left panel shows the O VI 1032 Å and 1037 Å. The middle panel shows the Lyα, [O V], O V], N III lines in both primary and redundant wavelengths. The primary (991.8 Å–986.1 Å) and redundant wavelengths (1212.5 Å–1217.7 Å) are represented in the upper and bottom axes in the middle panel, respectively. The right panel shows the C III line.

3. THREE-DIMENSIONAL RECONSTRUCTION

A three-dimensional reconstruction of the 2001 December 13 CME has been made based on O VI 1032 Å, Lyα 1216 Å, and C III 977 Å observed from 14:56 UT to 19:16 UT. Briefly, for each pixel along the UVCS slit, we first determine the velocity components in the plane of the sky for each exposure by dividing the difference between the eruption time and the time of the exposure into the difference in position between the pixel and the lcation of the eruption. The observed Doppler shift provides the line-of-sight velocity component for each pixel in each exposure. When different structures are superposed along the line of sight, they may show up as separate velocity components and can thus be separated into, for instance, structures on the front and back sides of the expanding CME (Lee et al. 2006) which were separated with multiple Gaussian fits. We then use the two plane-of-the-sky velocity components and the line-of-sight velocity to project the structure forward in time, adding in the material observed in each successive exposure. For this event, due to the 300 s exposure time, blobs with different properties were sometimes superposed in the same pixel during the same exposure. The velocities in the plane of the sky would cause those blobs to be superposed at later times in the two-dimensional projection onto the plane of the sky, but the different line-of-sight components of the blobs make it possible to separate them in the three-dimensional structure. Our method essentially assumes that the expansion is self-similar. This assumption is checked by comparing the projection of the three-dimensional structure onto the plane of the sky to LASCO images at later times. We use the same assumptions as the recent three-dimensional reconstruction of UV lines for the 2002 April 21 CME observed by UVCS by Lee et al. (2006) who give a detailed description of the method. This model has two key assumptions. One is homologous expansion in all directions. The other is that the line-of-sight velocities are only caused by the material's expansion, rather than thermal or turbulent motions.

3.1. Pre-processing of the Data

We subtracted as background the average of 35 pre-CME exposures observed from 08:02 UT to 14:16 UT. The scattered Lyα continuum was eliminated by a linear equation for the background emission in the observed wavelength ranges. The Gaussian wings on the instrumental line profile were corrected by an iterative procedure (Kohl et al. 1997). Since the detector has some distortion, we evaluated the reference line center of the O VI and Lyα by Gaussian fitting after binning by three spatial bins along the slit using the pre-CME observations above. The line center of the C III was evaluated using the O VI line center.

3.2. Expansion Model

The onset position of the CME eruption is obtained from the position of NOAA 9973, which was located at 0.084 $R_\odot$ to the west (hereafter the x-coordinate) and 0.218 $R_\odot$ to the north (hereafter the z-coordinate) according to the EIT image at 14:24 UT. The position in the line-of-sight direction was thus -0.972 $R_\odot$ toward the Earth (hereafter the y-coordinate) assuming the Sun is a sphere ($R_\odot = 1$). First, we assume that each element of plasma moved in a straight line from the eruption site to the UVCS pixel where it was observed, as described above. Second, we assume that all material erupts at the same time and location, and has constant speed before reaching the UVCS slit at each spatial bin. This implies that the plasma reaching the slit during later exposures travels more slowly in the plane of the sky than the plasma that reaches the slit earlier. The ejection is spread out in both location and time, but only by about 100 arcsec and 10 min in time as estimated from the *TRACE* movie. Given the limitations of spatial resolution and cadence of the UVCS and LASCO data, the assumption of a single point in space and time is adequate.

3.3. Images from the Three-Dimensional Reconstruction

A movie has been made using a 40 $R_\odot$ cube with 0.1 $R_\odot$ pixels (see online version). The reconstructed movie shows the distributions of the O VI, Lyα, and C III emissions (Figure 5). The red, green, and blue colors correspond to the O VI, Lyα, and C III emission, respectively. The yellow (O VI and Lyα), sky (Lyα and C III), violet (O VI and C III), and white colors (O VI, Lyα, and C III) show the overapping features of those lines. At the beginning of the observation, 14:56 UT and 15:01 UT, the blue-shifted components of C III emission were detected at the end of the wavelength range of this data panel (marked [b] in Table 3). This could underestimate the line-of-sight velocity to the Earth in the reconstructed movie.

Table 2
Line Intensities of the O VI, O V, and Electron Density

	O VI					O V]			$n_e(\times 10^6)$	$N_e(\times 10^{16})$
Blob No.	I_{1032}	$V_{\rm LOS}$	$V_{1/e}$	T_k	Depth	I_{1032}/I_{1037}	I_{1218}	I_{1213}/I_{1218}	O V	LASCO	LASCO
A	34.0[a]	−286	58	33	0.858	2.75 ± 0.14	···	···	···	2.04[b]	13.6
	39.4[a] $\chi^2 = 0.9$	−459	97	91							
B.1	261.6[a]	−286	81	63	1.217	2.43 ± 0.15	···	···	···	1.31[b]	12.4
	132.0[a] $\chi^2 = 3.7$	−459	112	121							
B.2	307.7 $\chi^2 = 0.9$	−487	58	33	0.367	2.78 ± 0.19	70.8 ± 7.0	···	···	5.14[b]	14.6
B.3	129.1 $\chi^2 = 2.8$	−260	90	78	0.566	2.05 ± 0.15	37.5 ± 5.1	···	···	2.38[b]	14.7
C.1	81.3 $\chi^2 = 0.2$	−457	56	30	0.394	3.03 ± 0.32	···	···	···	3.21[b]	9.68
C.2	118.8 $\chi^2 = 3.1$	−346	57	31	0.401	1.86 ± 0.13	35.6 ± 4.9	···	···	5.59[b]	17.1
C.3	574.7 $\chi^2 = 4.8$	−263	71	49	0.501	2.53 ± 0.09	62.5 ± 6.5	0.57 ± 0.11	$1.28^{+0.49}_{-0.35}$ [c]	5.88[b]	22.4
C.4	621.4 $\chi^2 = 14.8$	−234	87	73	0.613	2.03 ± 0.07	39.5 ± 5.2	0.57 ± 0.21	$1.25^{+1.08}_{-0.53}$ [c]	5.23[b]	24.3
C.5	71.1[a]	−66	38	14	0.652	1.98 ± 0.07	49.5 ± 5.8	0.47 ± 0.12	$1.64^{+0.81}_{-0.46}$ [c, b]	5.73	28.3
	439.2[a] $\chi^2 = 3.6$	−239	54	28							
C.6	100.8[a]	−95	71	49	0.760	2.05 ± 0.10	95.2 ± 8.1	0.10 ± 0.04	$11.2^{+10.9}_{-3.74}$ [c, b]	3.67	21.1
	184.0[a] $\chi^2 = 2.0$	−239	36	13							
D.1	176.3 $\chi^2 = 7.5$	−350	68	45	0.537	2.34 ± 0.14	54.7 ± 6.1	···	···	3.70[b]	15.0
D.2	167.3 $\chi^2 = 10.8$	−321	48	22	0.378	1.83 ± 0.14	43.3 ± 5.4	0.63 ± 0.17	$1.06^{+0.71}_{-0.39}$ [c]	6.39[b]	18.2
D.3	142.0 $\chi^2 = 4.5$	−297	30	8.7	0.234	2.79 ± 0.22	86.7 ± 7.7	0.30 ± 0.06	$3.08^{+0.88}_{-0.72}$ [c, b]	1.23	19.9
D.4	82.3 $\chi^2 = 3.8$	−297	45	20	0.350	3.43 ± 0.42	52.5 ± 6.0	0.37 ± 0.10	$2.31^{+1.11}_{-0.64}$ [c]	7.35[b]	19.4

Notes.
I: Intensity (10^8 photons cm^{-2} s^{-1} sr^{-1}). $V_{\rm LOS}$, $V_{1/e}$: km s^{-1}. T_k: 10^5 K. Depth : line-of-sight depth in $R_\odot$ unit evaluated by (FWHM of the O VI) × (travexl time from the source region to UVCS slit).
[a]Two-Gaussian fit. [b]The adapted electron number density for heating model. [c]The lower limit of electron density evaluated by [O V]/O V].

Table 3
Line Intensities of the Lyα, C III, C II, and N III

	Lyα				C III			C II (Int.)		N III (Int.)	
Blob No.	$I_{\rm Ly\alpha}$	$V_{\rm LOS}$	$V_{1/e}$	T_k	$I_{\rm CIII}$	$V_{\rm LOS}$	$V_{1/e}$	1036.34 Å	1037.02 Å	989.80 Å	991.58 Å
A	4351.8 $\chi^2 = 222.4$	−380	90	4.9	142.6[b]±5.5	···	···	2.6 ± 0.7	3.2 ± 0.8	···	48.9[d]±3.2
B.1	1776.9 $\chi^2 = 72.7$	−425	64	2.5	334.3[b]±8.5	···	···	7.7 ± 1.3	20.5 ± 2.1	···	42.0 ± 1.4
B.2	786.7 ± 23.2	···	···	···	··· [b]	···	···	···	9.0 ± 1.4	···	48.4 ± 3.2
B.3	5649.5 $\chi^2 = 51.8$	−325	80	3.9	397.6 ± 9.3	···	···	5.8 ± 1.1	20.5 ± 2.1	···	23.8 ± 2.3
C.1	···	···	···	···	14.5 ± 1.8	···	···	···	···	···	···
C.2	2169.3 $\chi^2 = 4.1$	−393	70	3.0	285.2[b]±7.8	···	···	···	···	6.3 ± 1.2	20.5 ± 2.1
C.3	1226.5[a]	−344	56	1.9	220.5[a]	−132	30	···	12.6 ± 1.6	···	26.0 ± 2.4
	487.3[a] $\chi^2 = 34.1$	−231	35	0.74	195.6[a] $\chi^2 = 4.0$	−193	[c]				
C.4	1254.3[a]	−321	67	2.7	40.4[a]	−41	[c]	···	9.3 ± 1.4	···	18.1 ± 2.0
	891.9[a] $\chi^2 = 22.0$	−208	49	1.5	239.1[a] $\chi^2 = 7.4$	−193	17				
C.5	337.5[a]	−317	41	1.0	72.6[a]	−46	18	···	12.2 ± 1.6	···	29.3 ± 2.5
	1291.2[a] $\chi^2 = 31.9$	−136	45	1.2	226.1[a] $\chi^2 = 3.7$	−198	[c]				
C.6	425.9[a]	−317	48	1.4	75.4[a]	−76	31	···	5.0 ± 1.0	···	21.4 ± 2.1
	565.0[a] $\chi^2 = 30.9$	−114	35	0.74	190.4[a] $\chi^2 = 11.4$	−198	[c]				
D.1	1442.6 $\chi^2 = 9.6$	−366	39	0.92	285.8 ± 7.9	···	···	···	···	···	21.8 ± 2.2
D.2	1441.0 $\chi^2 = 11.6$	−344	37	0.83	178.7 ± 6.2	···	···	3.8 ± 0.9	6.6 ± 1.2	···	37.1 ± 2.6
D.3	2762.1 $\chi^2 = 34.6$	−340	41	1.0	312.0 ± 8.2	···	···	4.3 ± 1.0	6.3 ± 1.2	···	35.3 ± 2.8
D.4	1886.6 $\chi^2 = 19.5$	−317	39	0.92	142.2 ± 5.5	···	···	···	···	···	16.2 ± 1.9

Notes.
I: Intensity (10^8 photons cm^{-2} s^{-1} sr^{-1}). $V_{\rm LOS}$, $V_{1/e}$: km s^{-1}. T_k: 10^5 K.
[a] Two-Gaussian fit. [b] Observations at the edge of the observed wavelength range. Lower limit of the C III emission. [c] FWHM is within the instrumental width. Possibilities of b. [d] Possibly part of the Lyα continuum.

We present four views from the solar east–Earth (upper left), the solar east–backside of the Sun (upper right), the backside of the Sun (lower left), and the solar west (lower right). The reconstructed structure is extended toward the Earth, as indicated by the strong blue shifts. The views from the solar west (lower right) make it easy to understand the distribution of the three emission lines along the line of sight. In the CME front, the O VI and Lyα emissions are positioned close together (red, green, and a mixed yellow color). Following those, the Lyα and C III emissions are closer to the middle of the ejected CME plasma (green, blue, and a mixed sky color). The C III emission is seen in the innermost part of the reconstructed movie, in agreement with earlier indications of a core of cooler material (Akmal et al. 2001). The view from the backside of the Sun to the Earth (lower left panel in Figure 5) also shows the C III emission in the innermost part of the ejected CME material. The bright features of O VI, Lyα, and C III observed by UVCS show the arch (shell-like) structure in the view from the solar backside (see the movie and the image at the bottom left in Figure 5). Inside of the shell-like structure, it is much fainter and seems to

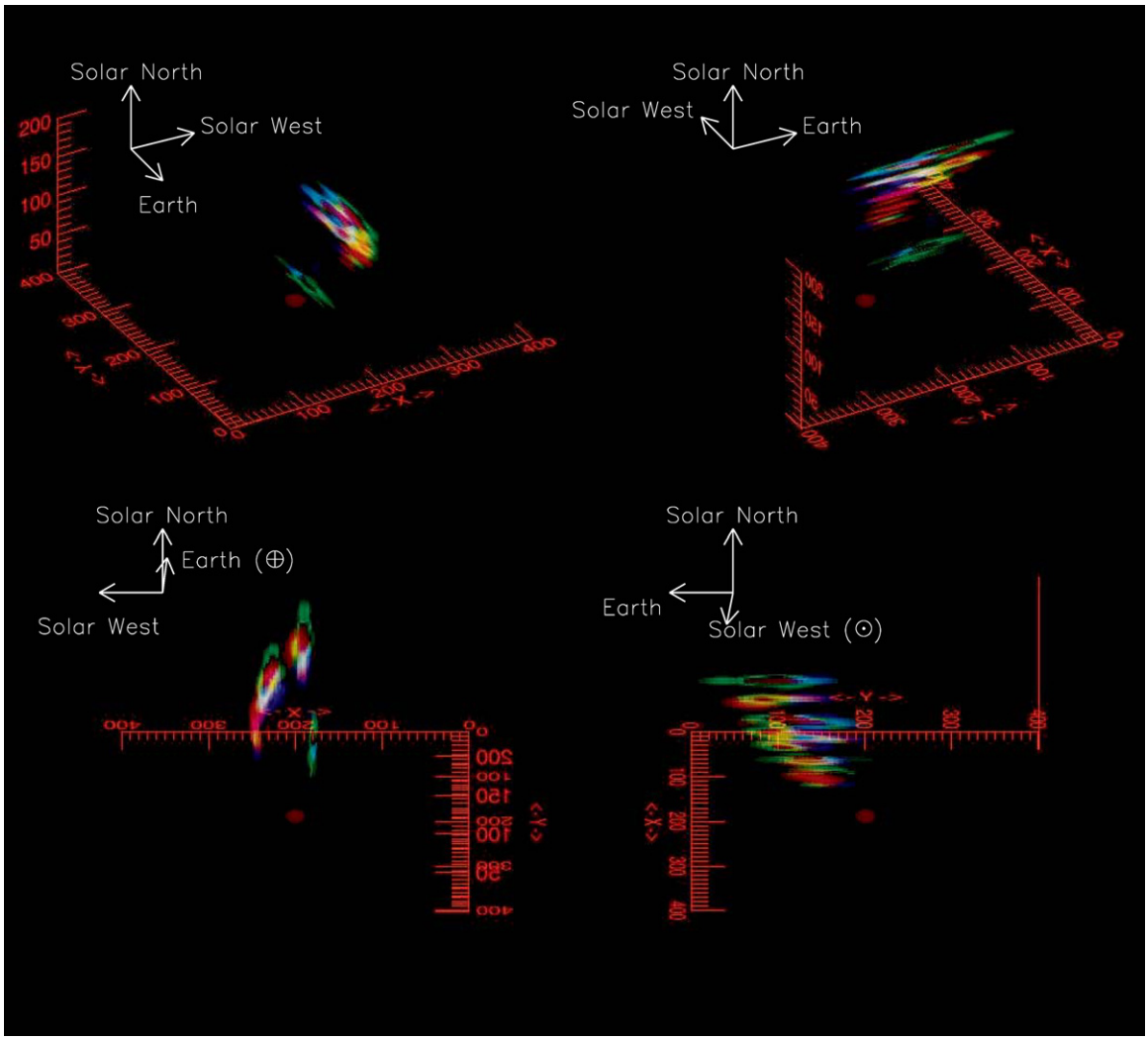

Figure 5. Three-dimensional distribution of the O VI (red), Lyα (green), and C III (blue) emission. Each grid presents 0.1 solar radius and the Sun is placed at the coordinate (x: 200, y: 200, z: 0). This figure is also available as an mpeg animation. The movie consists of two rotations; the first is the expansion of CME from 14:56 UT to 19:16 UT and the second rotation is at 19:16 UT.

(An mpeg animation of this figure is available in the online journal.)

be void. Krall (2007) compared the CMEs observed by SMM with a parameterized three-dimensional flux-rope model (Krall & St. Cyr 2006) and found that the CMEs observed by SMM in his study are consistent with the hollow flux-rope geometry. Our three-dimensional reconstruction looks like the hollow flux-rope structure, as best seen in the view from the back of the Sun.

4. ENERGY BUDGET

To investigate the energy balance of the 2001 December 13 CME plasma, we used the 14 blobs from the four exposures observed by UVCS from 14:56:19 UT to 15:12:48 UT (Table 1, see also Figure 4). The bright features of the 14 blobs occupy small spatial regions along the slit in one or more of the spectral lines. We analyze all the observed lines along the bright features which are marked with the white bar at the edge of the middle panel in Figure 4.

The procedure is much like that of Akmal et al. (2001), but for this event we have different constraints because different lines were observed, and because we use the three-dimensional reconstruction to constrain the depth along the line of sight. First, we evaluate the expansion of the CME plasma based on the *TRACE*, LASCO, and UVCS observations (Section 4.1). Second, we compute grids of models for a broad range of initial temperatures, densities, and forms of the heating function to calculate the ionization fraction along the CME expansion. The ionization fraction is evaluated by a time-dependent ionization code using density and temperature calculated from the expansion law (Section 4.2.2) as input and the energy equation (Equation (5) in Section 4.3). The ionization fractions are also used to compute the radiative cooling rate. At the final step of each model, the density, temperature, and ionization fraction are used to evaluate the line intensities (Equation (2)). Finally, the line intensities evaluated from each heating model are compared with the O VI, O V], Lyα, C III, C II, and N III line emission observed by UVCS.

The heating laws for fast solar wind (Allen et al. 1998), in which proton and electron rates differ, as well as a density-proportional heating rate are used to model the heating rates. The flux-rope model for interplanetary magnetic clouds (Kumar & Rust 1996) is also used to evaluate the energy balances of the ejected plasma. The heating rates in the models contain all forms of thermal energy input including wave dissipation, magnetic heating, and the divergence of thermal conduction,

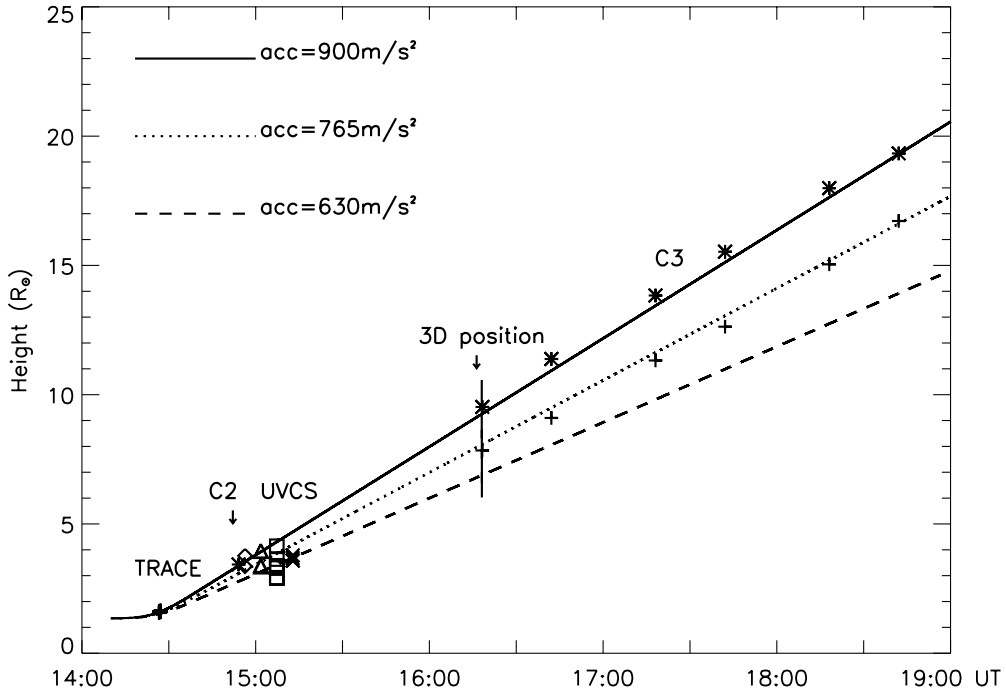

Figure 6. Expansion heights of the CME plasma. The stars and crosses for C3 represent the position of the upper edge of the left loop (where blob "A" is placed) and right loop (where blob "C" is placed) in the LASCO image in Figure 9. For the UVCS observation, the diamond represents blob A, the triangle represents blob B, the square represents blob C, and the mark "×" represents blob D. The solid line is the distance applied for blob A, the dotted line is the distance applied for blob B, and the dashed line is the distance for blobs C and D.

which we will consider in Section 6. Here we model the ejected plasma including radiative and adiabatic cooling to investigate the temperature evolution of the CME material with a time-dependent ionization state model. We describe the model in more detail in the following subsections.

4.1. Expansion Model

We use an acceleration profile to evaluate the height of the ejected plasma rather than the constant velocity that was used to make the three-dimensional reconstruction. Chen et al. (2006) showed that the distance of the two footpoints in the active region is related to the maximum expansion velocity of the CME flux rope. We determined the peak time of the acceleration, 14:25:00 UT, based on the distance of the two footpoints from *TRACE* 1600 Å observations. Then the start time of the expansion, 14:10:12 UT, was evaluated to match the heights of the CME plasma observed by *TRACE*, UVCS, and LASCO observations. Different slopes of the acceleration were used for each exposure. The applied accelerations are 900 m s^{-2} and 765 m s^{-2} for the A and B blobs, respectively, and 630 m s^{-2} for the C and D blobs. The *TRACE* 1600 Å observations also show that the brightening in the active region starts around 14:10 UT and increases slowly after that. The evaluated heights of the ejected CME plasma are presented in Figure 6.

4.2. Observational Constraints

Electron density, kinetic temperature, and line intensity are used to constrain the acceptable models for a broad range of initial temperature, density, and three heating functions for each of the 14 blobs. The electron density evaluated at the UVCS slit height is used to determine the electron density at each time in the expansion model and to evaluate the emission measure (EM). The kinetic temperature of Lyα is used as the upper limit to the temperature at the UVCS slit height. The observed line intensities are compared with the intensities obtained from the models.

4.2.1. Electron Density

The ratio of the [O v]/O v] lines is a reliable density diagnostic. This ratio has been used to determine the electron density of the ejected CME plasma, and it is most useful for densities of 10^6–10^7 cm^{-3} (Akmal et al. 2001). In this event, UVCS observed the [O v] forbidden line at 1213.85 Å and the O v] intercombination line at 1218.39 Å in several blobs, though the 1213.85 Å line could not be cleanly separated from the N III 991.85 Å line in most cases. For the seven blobs observed at 15:07 UT and 15:12 UT, the electron number densities were evaluated from [O v]/O v]. We present the line profiles of the three blobs C.5, C.6, and D.3 in Figure 7. Both primary and redundant wavelengths are presented together. The [O v] line may be contaminated by N III 991.58 Å, and while we attempted to remove the N III by assuming that its profile is the same as that of C III 977 Å, we consider the [O v] intensities to be upper limits and the density estimates to be lower limits. We use the electron number densities from the ratio of the [O v]/O v] for the three blobs C.5, C.6, and D.3 for the analysis of the heating rates and those are marked with [b,c] in Table 2. The electron density evaluated from the O v ratio and version 5.2 of CHIANTI (Dere et al. 1997; Landi et al. 2006) is presented with uncertainties in Figure 8. For other blobs, the electron number densities are evaluated from the column densities observed by LASCO, divided by the line-of-sight depth based on the O VI line emission. The three-dimensional reconstruction of the O VI lines shows the reconstructed width is similar to the CME width from the LASCO observation (Lee et al. 2006). We take the depth of the O VI line to be the FWHM multiplied by the travel time from the source region to the UVCS slit. The evaluated electron number density and column density were presented in Table 2.

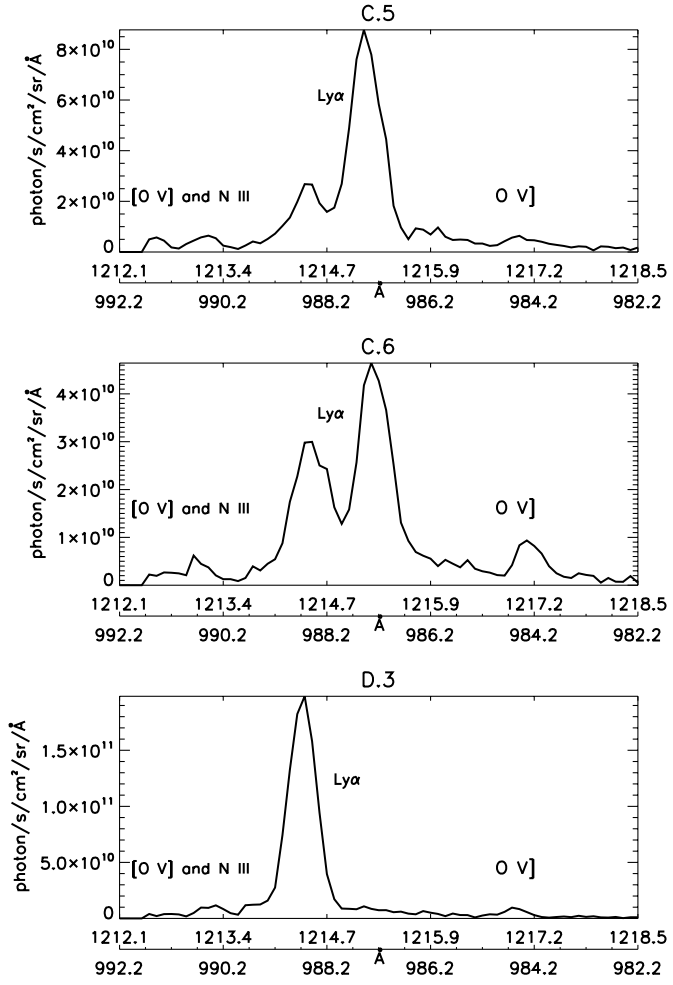

Figure 7. Lyα, [O v], O v], and N III line intensities of the blobs C.5, C.6, and D.3.

The LASCO C3 observation at 16:18 UT was used to evaluate the column density along the line of sight. Unfortunately LASCO did not observe this event when the [O v] and O v] lines were observed from 15:07 UT to 15:12:48 UT (refer to Figure 3). The three-dimensional reconstruction makes it possible to estimate the height and the angle with the plane of the sky. The heights of the UVCS blobs predicted by the constant velocity reconstruction are higher than their positions in the LASCO C3 image at 16:18 UT. We use the positions from the reconstruction using the observed acceleration to connect the UVCS blobs to the LASCO image. In Figure 9, the reconstructed positions of the observed blobs are presented with the LASCO C3 observation, and each box represents the A, B, C, and D blobs in Table 1. The reconstructed positions of blobs A−D are also indicated by "three-dimensional position" in Figure 6. Vourlidas et al. (2000) showed how the densities derived from LASCO increase with the angle with the plane of the sky due to the angular dependence of Thomson scattering. Plane-of-the-sky angles of 40°–50° were found for the observed blobs from the line-of-sight velocities. We used an angle with the plane of the sky of 45 ° to evaluate the column densities from the LASCO observation. The column densities were calculated by averaging the area of each box in Figure 9. After the column density was obtained, we scaled the density inversely with height squared to estimate the column density at the height of the UVCS observations.

4.2.2. Temperature and Line Intensity

The line widths obtained by the Gaussian fit for the 14 blobs contain the kinetic temperature and nonthermal (bulk velocity) components. The upper limits on the kinetic temperatures of O VI and Lyα are presented in Tables 2 and 3, respectively. Note that in the three-dimensional reconstruction, the line width is assumed to be caused by the material's expansion along the line of sight. Here we regard the kinetic temperature to be the upper limit of the electron temperature at the UVCS slit height as one of the criteria for selecting the acceptable models. The Lyα width constrains only the ion temperature in the Lyα emitting region since the O VI and Lyα generally do come from different regions. The temperature T_k is defined as

$$T_k = \frac{1}{2}\frac{m}{k}v_{1/e}{}^2, \quad (1)$$

where m is the mass of the ion and $v_{1/e}$ is the velocity derived from the Doppler half-width, $\triangle\lambda_{1/e}$. We subtract about 0.3 Å (3 pixels) in quadrature to account for the effect of the slit width of 0.298 Å (0.275 Å for the redundant channel).

Radiative and adiabatic cooling along with the heating rates are used to investigate the temperature evolution of the CME material in the time-dependent ionization state model. We use the expansion law $n_{uvcs}/(n_0 - n_{uvcs}) \propto (t/t_{uvcs})^{\alpha}$, which determines the adiabatic cooling rate ($L_{\rm adiabatic}$ in Equation (5)) from $T/n^{\gamma-1}$ (Akmal et al. 2001, see Section 4 in their paper). Initial densities (n_0) are examined from 3×10^8 cm^{-3} to 2×10^{11} cm^{-3} with initial temperatures from 1×10^4 to 6.3×10^6 K. t_{uvcs} is the duration time of the CME expansion from 14:10:12 UT (Section 4.1) to the UVCS observations. Using the density (n_{uvcs}) determined at the UVCS slit, 2.4 $R_\odot$, the expansion is assumed to be a power law. We adopt the power law of $\alpha = 3$, which means an expansion in both length and radius and a slower expansion at the earlier stages than the expansion with $\alpha = 1$ or 2. Since we do not know exactly how the CME has expanded from the origin to the solar corona, the power-law assumption adopted in earlier work (Akmal et al. 2001) is the simplest way to parameterize the density falloff with height. Also the choice of $\alpha = 3$ matches the observed slower expansion in the earlier stages. During the expansion of the CME plasma, the ionization fraction is evaluated from the time-dependent ionization state model. The ionization and recombination rates were taken from an updated version of the code of Raymond (1979). This atomic physics package computes the collisional ionization, radiative recombination and dielectronic recombination rates for astrophysically abundant elements, and the evolution of the ionization states of the elements was computed with the usual set of equations for the rate of change of each ionic fraction. The time-dependent ionization balance was used with solar photospheric abundances (Grevesse & Sauval 1998) to compute the radiative cooling rate (L_r in Equation (5)). Photospheric abundances were chosen because the knots we analyze are probably ejected prominence material, rather than coronal plasma. The computed ionization fraction is used to determine the line intensity. In coronal conditions with the isothermal assumption, the line intensity is expressed as follows (e.g., Ko et al. 2006):

$$I_{\rm line} = \frac{1}{4\pi}\frac{n_{\rm el}}{n_{\rm H}}\int \epsilon(T_e)d{\rm EM}(T_e) \text{ photons cm}^{-2}\text{s}^{-1}\text{sr}^{-1}, \quad (2)$$

where $n_{\rm el}/n_{\rm H}$ is the abundance of the element relative to hydrogen. In our model, the line intensity is calculated for a

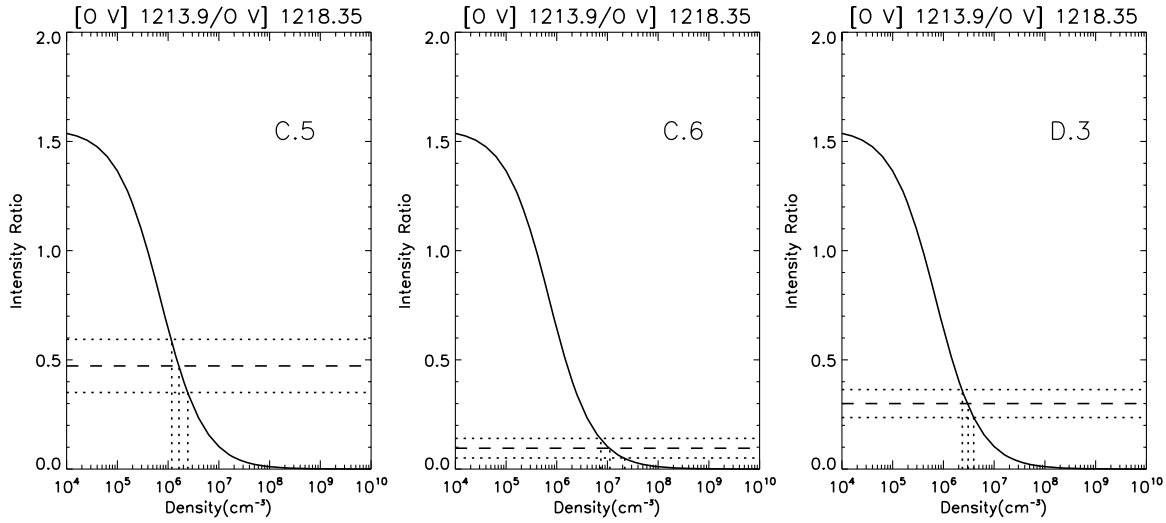

Figure 8. Observed line ratio of the [O v]/O v] and the electron number density evaluated from CHIANTI 5.2.

single temperature at any time. So we use the EM ($= 0.8 n_e N_e$) instead of dEM without the integral. 0.8 is the hydrogen abundance relative to the electron density, n_e is the electron number density determined from the O v lines or from the LASCO observation divided by line-of-sight depth (see Section 4.2.1), and N_e is the column density determined from the LASCO image (see Section 4.2.2). $\epsilon(T_e)$ is the emissivity, which is defined as

$$\epsilon(T_e) = \frac{n_{\rm ion}}{n_{\rm el}}(T_e) q_{\rm line}(T_e), \quad (3)$$

$n_{\rm ion}/n_{\rm el}$ is the ionization fraction. $q_{\rm line}$ is the collisional electron excitation rate given by

$$q_{\rm line}(T_e) = \frac{8.63 \times 10^{-6}}{\sqrt{T_e}} \frac{\Omega_{ij}}{w_i} e^{-E/kT_e}, \quad (4)$$

where Ω_{ij} is the collision strength taken from version 5.2 of CHIANTI and w_i is the statistical weight.

The observed line intensities are compared with the line intensities predicted from the three heating models (see Section 4.3). To match the O VI blobs, we use the ratio of the O VI/O V] which allows a factor of two margin because the density obtained from O V may not pertain to the O VI emitting gas. To match the Lyα, C III, C II, and N III blobs, we require that the predicted emission is at least as large as the observed values but is three times smaller than the observed intensity. We allow this margin because of the difficulty in evaluating the EM, given that we do not have a density from the O V lines for this cooler gas, and the combination of line-of-sight depth with LASCO column density carries a greater uncertainty. When the C III was observed near the edge of the panel, we exclude this constraint. In cases where the O VI/O V] ratio is not well matched (C.4 and D.4 for the heating model of Kumar & Rust, marked by [c] in Table 4), we use the same constraints for the Lyα, C III, C II, and N III blobs. We present the detailed constraints and the evaluated energy in Table 4.

4.3. Heating Model

Earlier UVCS observations of CMEs found evidence that the ejected plasma is heated long after the eruption (Akmal et al. 2001; Ciaravella et al. 2001). We investigate the heating rate for the following three heating models (see Section 4.3.1 and Section 4.3.2). The heating rate, H, enters the energy equation,

Figure 9. Reconstructed positions of the 14 blobs are presented in the LASCO C3 image.

$$\frac{5}{2} nk \frac{dT}{dt} = -n_e n_p (L_r + L_{\rm adiabatic} - H), \quad (5)$$

where n is the density of both protons and electrons. k is the Boltzmann constant, and n_e and n_p are electron and proton density, respectively. L_r and $L_{\rm adiabatic}$ are the radiative cooling rate and the adiabatic cooling rate, respectively. H includes all contributions to the heating, such as wave dissipation, magnetic reconnection, turbulent heating or the divergence of conductive flux, or shock waves generated by the reconnection outflow (Shiota et al. 2005). We combine turbulent heating with wave dissipation, so

$$H = H_{\rm wave} + H_{\rm mag} + H_{\rm cond} + H_{\rm shock}. \quad (6)$$

We have used the physical value of the specific heat ratio $\gamma = 5/3$. Smaller values of γ are often used in coronal models with the heating rate set equal to zero in order to obtain plausible temperature profiles without knowledge of the heating rate. In this case we aim to derive the heating rate, so the value of γ for a monatomic gas is appropriate.

Table 4
Energy Budgets for the Three Heating Models

Blob No.	O VI (H1)							Lyα, C III, CII, N III (H2)			
	$Q \propto Q_{AHH}$		$Q \propto n$		$Q \propto Q_{KR}$			$Q \propto Q_{AHH}$		$Q \propto n$	
	H.E.	T.E.	H.E.	T.E.	H.E.	T.E.	h	H.E.	T.E.	H.E.	T.E.
A	4.4–444	0.1–9.7	5.1–51	0.1–0.9	87–106	0.5	81–84	11	0.3	8.0 [d]	0.1 [d]
B.1	129–420	3.0–9.4	57–90	1.0–1.6	71–72	0.3	77	13–21[a]	0.3–0.5 [a]	14–27[a]	0.3–0.4[a]
B.2	58–65	1.3	57	1.0	71–77	0.3	77–78	5.5–5.8	0.1	9.0	0.2
B.3	15–89	0.3–2.0	9.0–57	0.2–1.0	71–77	0.3	77–78	5.2–5.5 [b,d]	0.1[b,d]	9.0 [e]	0.2 [e]
C.1	18–225	0.4–5.0	25–100	0.4–1.7	57–102	0.2–0.4	71–82	2.5–45	0.07–1.0	4.0–25	0.07–0.4
C.2	4.4–44	0.1–1.0	6.3–40	0.1–0.7	57–70	0.2–0.3	71–75	3.7–4.1	0.1	6.3	0.1
C.3	60–68	1.4	63	1.1	62–70	0.2–0.3	73–75	3.6–4.3	0.1	6.3	0.1
C.4	74	1.6	63	1.1	70[c]	0.3[c]	75[c]	4.2–4.7[d]	0.1[d]	6.3[d]	0.1[d]
C.5	138–144	3.4	63	1.1	57–82	0.2–0.3	71–78	5.4–5.7	0.1	6.3	0.1
C.6	18–45	0.3–0.8	16–40	0.3–0.7	57–82	0.2–0.3	71–78	4.0–4.5[d]	0.09[d]	4.0[d]	0.07[d]
D.1	51–56	1.1	17–44	0.3–0.7	58–71	0.2	70–74	4.9–5.3	0.1	6.9	0.1
D.2	9.0–57	0.2–1.0	6.9–44	0.1–0.7	58–105	0.2–0.3	70–81	4.7–5.2[d,e]	0.1[d,e]	6.9[d,e]	0.1[d,e]
D.3	6.7–65	0.1–1.3	6.9–44	0.1–0.7	58–59	0.2	70	6.2–6.3[d]	0.1[d]	6.9[d]	0.1[d]
D.4	5.1–32	0.09–0.5	4.4–27	0.07–0.5	58–218 [c]	0.2–0.7 [c]	70–90[c]	4.0–4.6[e]	0.09[e]	4.4	0.07

Notes.
T.E. and H.E. : thermal energy and heating energy (1.0×10^{14} erg g^{-1}) assuming 10% helium. h : the percentage of the lost magnetic energy appearing as heat. [a] Does not satisfy the C II observations. [b] Does not satisfy the N III observations. [c] Does not satisfy the O VI / O V constraint. [d] (and [e]) Does not satisfy the C II $< 3 \times$ C II (and C III) criterion.

We use a wide range of heating rates with three forms of the heating function. Two of them are taken from parameterized heating rates for the solar corona, and the third is from the CME model of Kumar & Rust (1996).

4.3.1. Parameterized Heating

The heating law for fast solar wind (Allen et al. 1998), in which proton and electron heating rates differ (hereafter denoted as $Q \propto Q_{AHH}$), and the density-proportional heating (hereafter $Q \propto n$) are used to evaluate the heating rates.

The density-proportional model was chosen as in Akmal et al. (2001) to provide a heating rate that declines more gradually than the exponential rate of Allen et al. (1998). It implies no specific physical mechanism, but for instance saturated thermal conduction with a constant temperature gradient might give such heating. Shiota et al. (2005) have described how the impact of reconnection outflows on the trailing edge of a CME core can generate slow mode shock waves that travel around and into the core. Lacking knowledge of the evolution of the reconnection outflow or the location of the shock dissipation, we cannot predict the functional form of this heating rate, but it is plausible that it declines on a timescale comparable to the travel time to the height of the UVCS slit.

For the model $Q \propto Q_{AHH}$ the proton and electron heating rates (Q_p and Q_e) are defined as

$$Q_e = Q_{e0} e^{-(r-R_S)/\sigma_e},$$
$$Q_p = Q_{p0} e^{-(r-R_S)/\sigma_p} + q00 \left(\frac{R_S}{r}\right)^4 (1 - e^{-(r-R_S)/5R_S}) \quad (7)$$

(Allen et al. 1998). We consider a constant heating rate with an exponential falloff with scale height 0.7 $R_\odot$ ($\sigma_{e,p}$). Q_{e0}, Q_{p0}, and $q00$ are the strength of heating terms taken from the SW3 model in their paper. r is the distance from the initiation site and R_S is solar radius. The temperature changes due to the proton and electron interaction are considered for the heating model $Q \propto Q_{AHH}$. We model the heating functions for a range of constants of proportionality covering three orders of magnitude.

4.3.2. Magnetic Heating

The magnetic clouds in ICMEs generally have simple magnetic structures that can be fitted with a Lundquist solution (e.g., Lynch et al. 2005), a minimum energy state for a given magnetic helicity. To reach this state, the complex, stressed magnetic configuration of the erupting structure must relax by dissipating magnetic energy. The MHD model of Lynch et al. (2004) shows that this occurs by the time the CME reaches about 15 $R_\odot$. MHD models do not generally show predicted heating rates, and in any case the heating is unlikely to be uniform throughout the CME structure. However, the model of Lynch et al. (2008) indicates that about 15% of the total change in magnetic free energy goes into kinetic energy.

In order to parameterize magnetic heating we use the flux-rope model for interplanetary magnetic clouds of Kumar & Rust (1996; hereafter $Q \propto Q_{KR}$). The model predicts that the magnetic energy goes into overcoming solar gravity, kinetic energy for the CME expansion, and heating energy. An important feature of the model is its use of the principle of conservation of magnetic helicity. It suggests that the magnetic energy stored in an expanding plasma should decrease with expansion ($H_m \propto$ length scale $\times U_m$), where H_m is the magnetic helicity and U_m is the magnetic energy. Kumar & Rust (1996) assume that the flux rope evolves through a self-similar series of axisymmetric states each having the lowest energy consistent with conservation of magnetic helicity. The assumption of self-similar axisymmetric expansion may be adequate when the CME is much larger than the source region (Uralov et al. 2005), but it is not likely to be accurate at small heights (Akmal et al. 2001). Kumar & Rust (1996) also assume that magnetic energy is dissipated in the expansion process, though they do not identify the dissipation mechanism in detail.

We use the length scale $l = 2\pi a$ where a is the radius of the flux rope (Kumar & Rust 1996; their Figure 2). We use the distance of the CME plasma from the initiation site as the radius "a". Kumar & Rust found that the change of magnetic energy is $dU_m = U_m(l_0) l_0 dl / l^2$ and that as the CME expands the magnetic energy lost is partitioned between kinetic

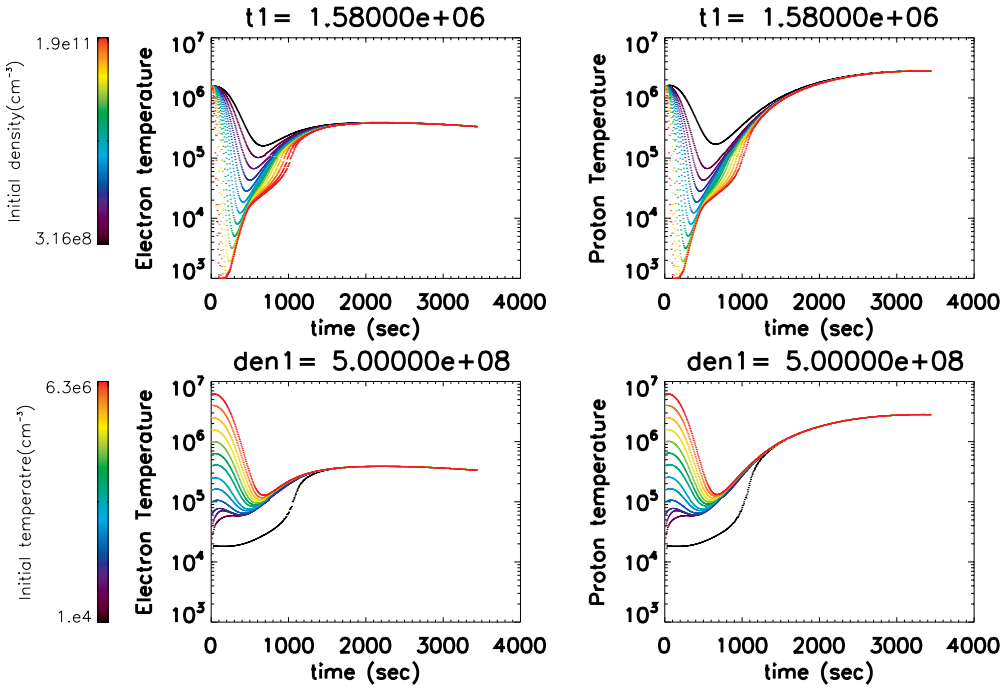

Figure 10. Temperature evolution of the protons and electrons of the model Q_{AHH} for matching the O VI and O V] line intensities of the blob C.5.

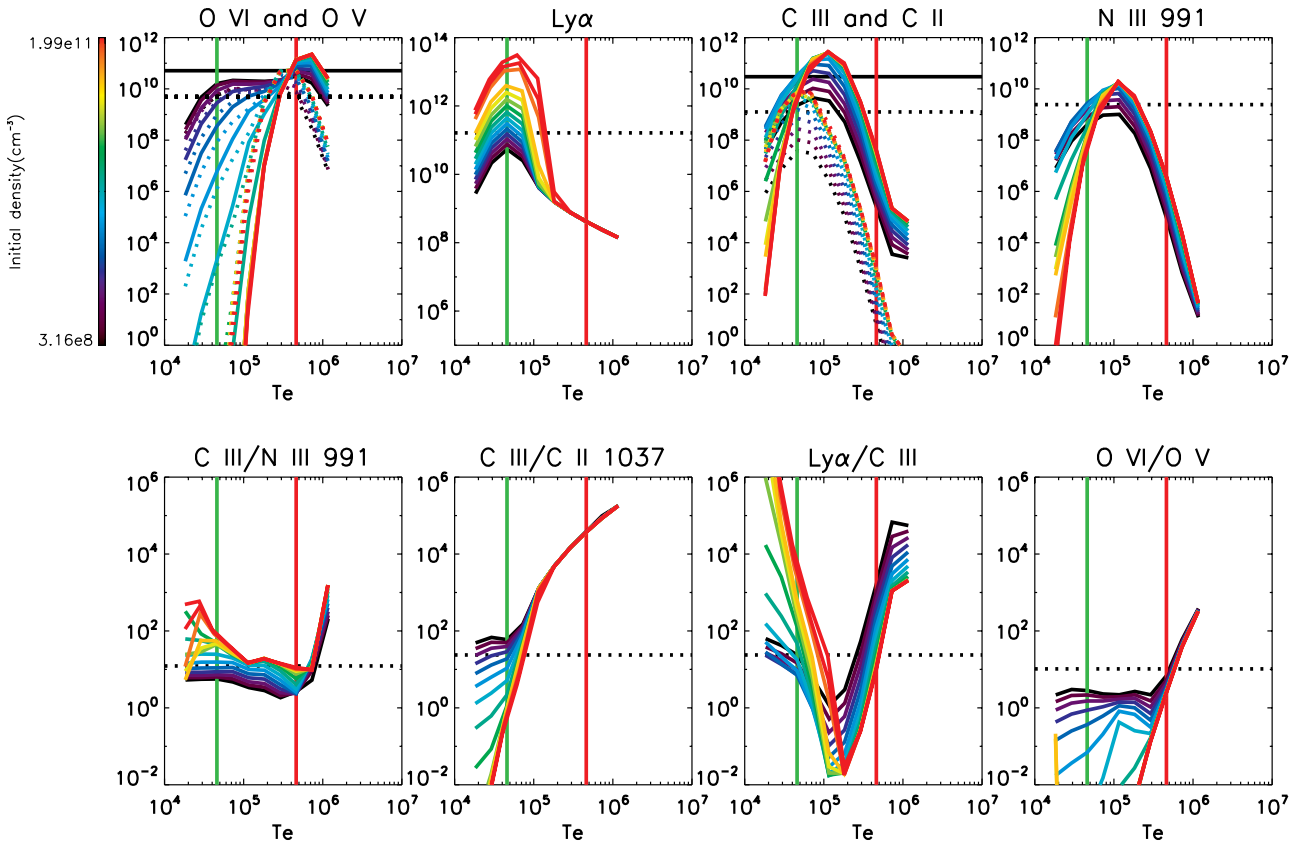

Figure 11. Line intensities when different heating rates are applied to the heating model $Q \propto Q_{AHH}$. The rainbow colors indicate different densities. The horizontal lines are the observed values. In the first panel, the solid and dotted lines are the observed O VI and O V values, respectively. In the upper third panel, the solid and dotted lines are for the C III and C II lines, respectively. The green vertical line is the temperature that matches the Lyα, C III, C II, and N III emissions and the red vertical line is the temperature that matches the O VI/ O V and O VI emissions.

+ gravitational and thermal energies according to a parameter $s = 1 - \sin(\theta_0)/\pi$ that may vary from one event to another. θ_0 is an effective toroidal angle (see Figure 5 in their paper). As stated in their paper, the kinetic energy of major radial expansion about the center of mass is same as the kinetic energy of the center of mass (the kinetic energy of the minor radial

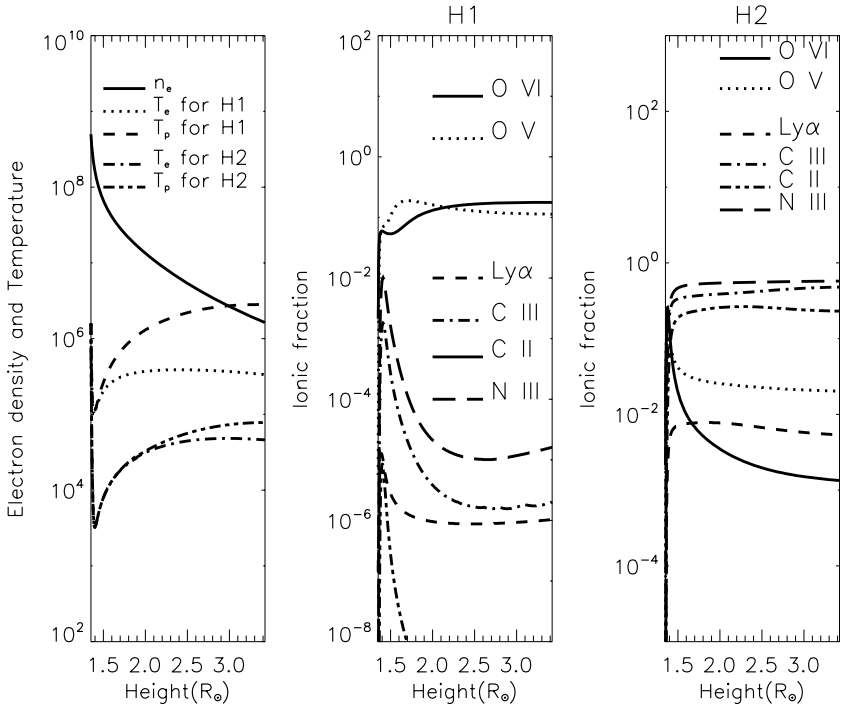

Figure 12. Evolution of the density, temperature, and ionization states for one of the acceptable models for blob C.5.

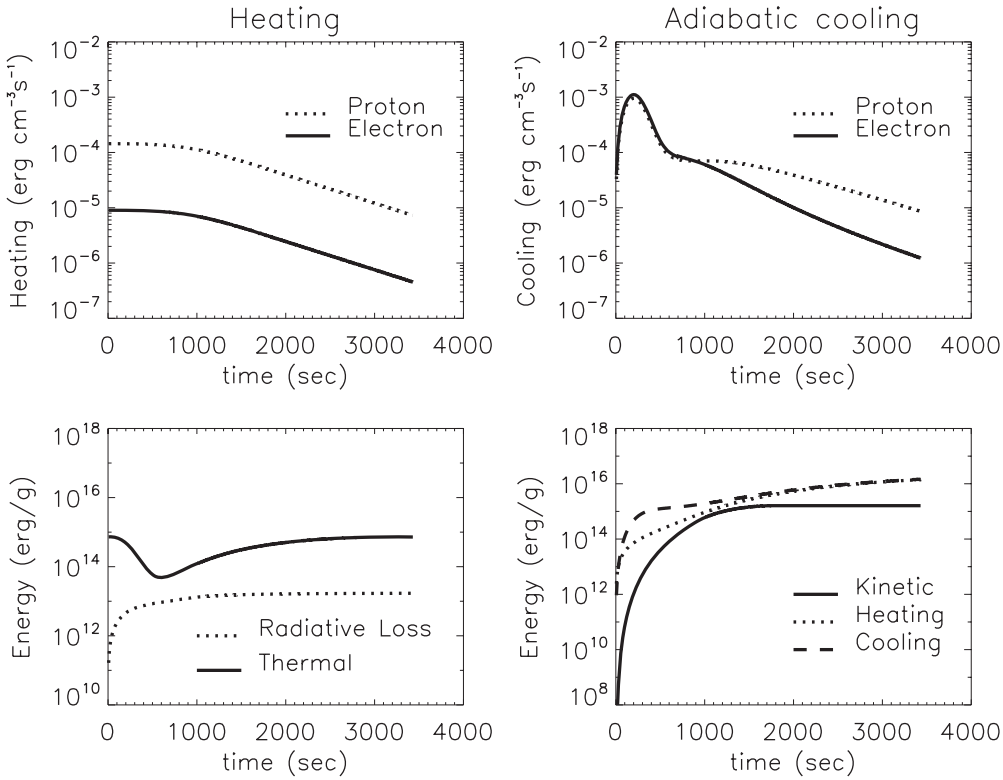

Figure 13. Energy budgets for H1, $Q \propto Q_{\rm AHH}$.

expansion is negligible for a large aspect ratio toroidal cloud) and the force acting on the center of mass is maximum on the leading edge of the flux rope. With twice the center of mass kinetic energy derived by integrating the motion of the center of mass from the initial distance to the leading edge of the flux rope ($\theta_0 \leqq \pi/2$), they presented energy conservation as $dQ + dU_m + dU_G + dU_{KE} = 0$. Using energy conservation, we derive the heating energy during the expansion of the CME plasma. If dU_G is the change in gravitational energy and dU_{KE} is the change in kinetic energy, then

$$dQ = -h dU_m \tag{8}$$

where $h = (1 + dU_G/dU_m + dU_{KE}/dU_m)$ is the fraction of the lost magnetic energy appearing as heat. We find the

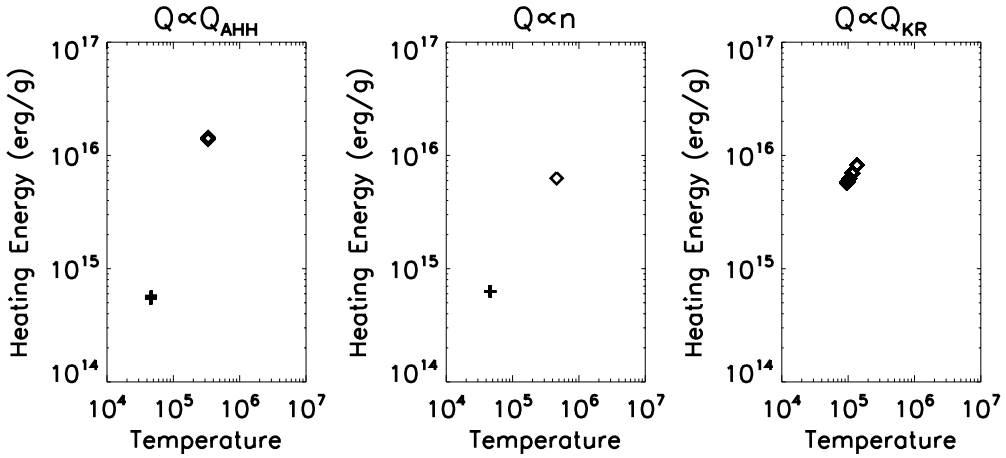

Figure 14. Heating energy. ◇ and + are for H1 and H2, respectively.

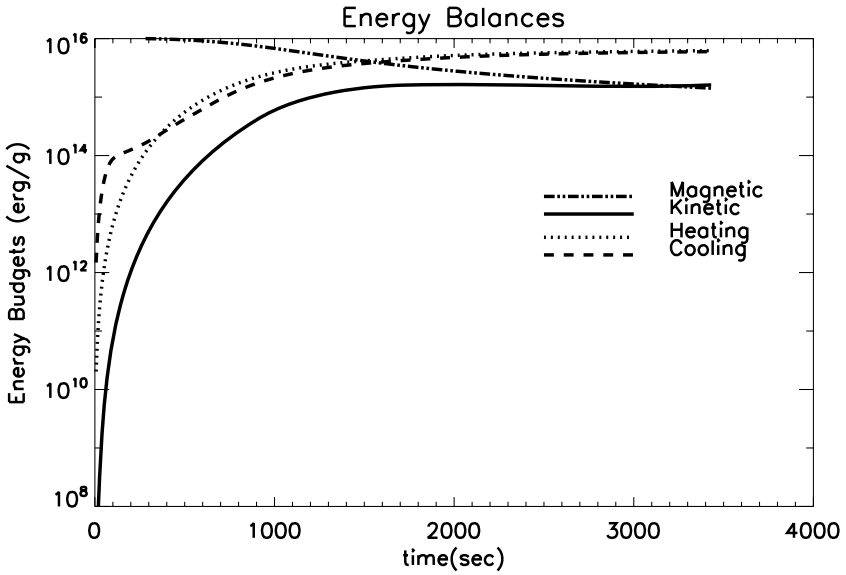

Figure 15. Energy balance of the Kumar and Rust's heating model.

kinetic and gravitational energy from the velocities and distances explained in Section 4.1. The final kinetic energy and the initial gravitational energy are fixed by the observed velocity and initial height of CME plasma, respectively. We find the heating rates to match the observations for θ_0 in the range of 10–90 °. The blobs we observe appear to be part of the ejected prominence and as such they are part of the flux rope. The energy budgets we obtain pertain specifically to these blobs but lacking any reason to assume otherwise, we believe that the heating is uniform throughout the flux rope.

5. ENERGY BALANCES

5.1. Temperature Evolution

Figure 10 shows the temperature evolution of both protons and electrons when one of the acceptable heating rates is applied for matching the O VI and O V] line intensities of blob C.5. The applied heating rate is 63 times that for a fast solar wind model ($Q \propto Q_{\rm AHH}$). The upper two panels show the proton and electron temperature evolutions for all applied initial densities ($3.16\times10^8-1.99\times10^{11}$ cm^{-3}) for a particular initial temperature, 1.58×10^6 K. The higher initial densities (red and yellow ranges in the rainbow colors) drop more rapidly than the lower initial densities, but all initial densities reach the same temperature at the time of the UVCS observation. The lower two panels show the same feature as that above for all applied initial temperatures ($1.0\times10^4-6.3\times10^6$ K) at that particular initial density, 5×10^8 cm^{-3}. The proton temperature increases more than the electron temperature because of the different heating rates for protons and electrons (see Section 4.3.1). The temperatures drop rapidly at lower heights and in the earlier stages of the expansion, and then they remain fairly constant depending on the heating rates. This is a similar result to that of Akmal et al. (2001) (see Section 5.2 and Figure 12 in this paper; also see Figure 12 in their paper). Our models show that the temperatures at coronal heights are determined by the heating rates rather than the initial temperatures and densities. In Figure 11, we present the line intensities (upper panels) and the line ratios (lower panels) for all initial densities with the temperature predicted from a range of heating rates which are 0.63–630 times Q_e and Q_p of the $Q \propto Q_{\rm AHH}$ (initial temperature $= 1.58\times10^6$ K). The temperatures that agree with the O VI, Lyα, C III, C II, and N III emissions indicate that different heating rates are required for those ions. For this model, the heating rates for the O VI blobs and for the blobs of cooler ions are respectively 63 times and 2.5 times that of the fast solar wind model. Hereafter H1

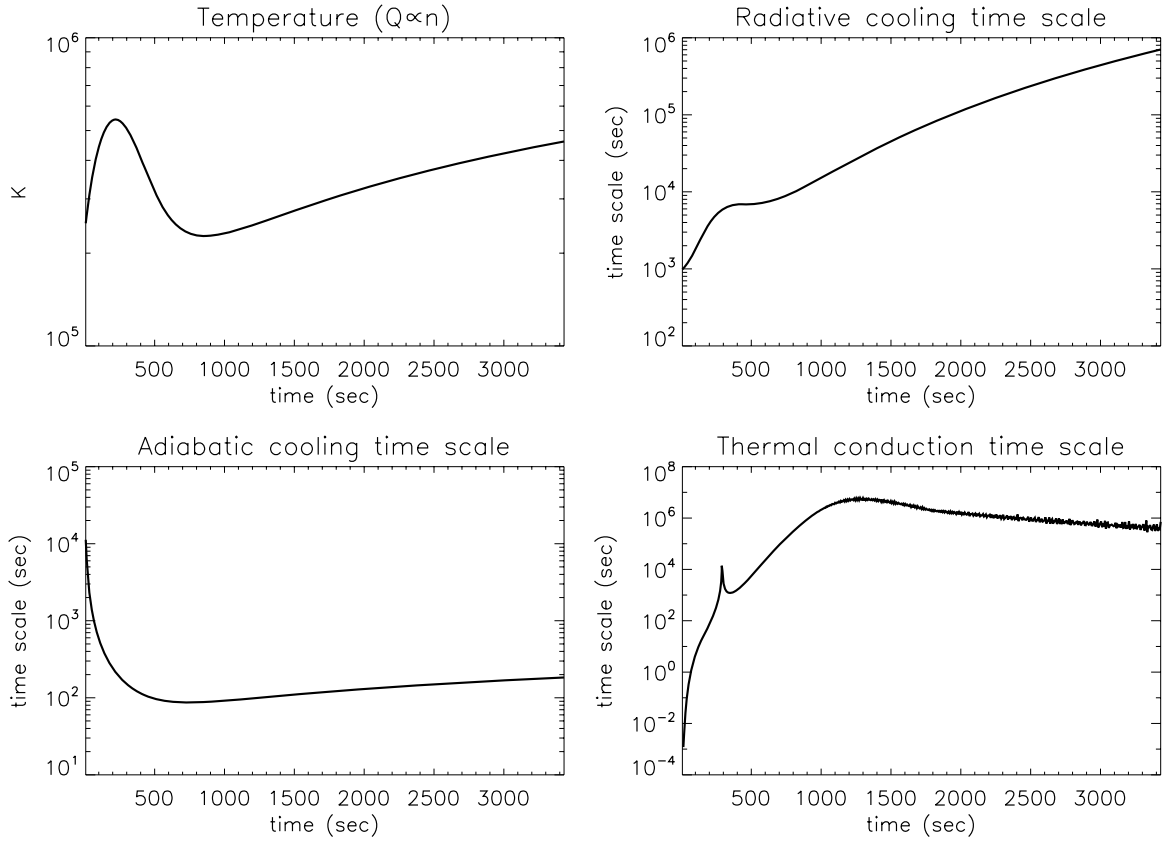

Figure 16. Timescale of radiative cooling, adiabatic cooling, and thermal conduction.

represents the heating rates that match the O VI emission and H2 represents the heating rates for matching the Lyα, C III, C II, and N III emission.

5.2. Heating, Cooling, and Energy Budget

Figure 12 shows the evolution of the temperature, density, and ionization state for one of the acceptable models explained above. The temperature and ionization fractions change rapidly at lower heights. For the H1 models, the O VI and O V ionic fractions maintain higher values after the rapid increase at lower heights, but the fractions of other ions, Lyα, C III, C II, and N III emissions, decrease again (the middle panel in Figure 12). For the H2 model, the fractions of the O VI and O V decrease and the others maintain their fractions (the right panel in Figure 12). The rapid change in the ionic fraction at low heights reflects the change in the electron temperature when they are in ionization equilibrium. In contrast, at heights higher than 2 $R_{\odot}$, the rapid expansion tends to "flatten" the ionic fraction indicating that the ions are frozen-in. The outflowing ions flow too fast and the density is too low for them to exchange electrons between neighboring ionization states from collisions. Figure 13 shows the heating and cooling rates for the H1 model in the upper panels. The adiabatic cooling rate increases rapidly at the earlier stages (the upper right in Figure 13). This drastic cooling rate requires that continuous heating increases the temperature to match the observations. The thermal and radiative loss energies are smaller than the heating and adiabatic cooling energies. The heating energies for the acceptable models for each of the three heating functions are shown in Figure 14. The heating rates for the O VI (H1) and for the Lyα, C III, C II, and N III (H2) observations are presented as diamonds and crosses, respectively. H1 is over ten times higher than H2 and the $Q \propto Q_{\rm KR}$ model does not match the observations for the Lyα, C III, C II, and N III blobs. The integrated heating energy balances cooling energy, and the total heating is greater than the kinetic energy in both the $Q \propto Q_{\rm AHH}$ and $Q \propto Q_{\rm KR}$ models, as shown in the lower right in Figure 13 and Figure 15. The Kumar & Rust model predicts that the magnetic energy decreases while conserving magnetic helicity.

6. DISCUSSION

In Table 4, we present the heating and thermal energy for all 14 blobs. The kinetic energy of this CME is 1.6–3.3$\times 10^{15}$ erg g^{-1} which is evaluated from the velocity of the CME plasma at the UVCS slit, 2.4 $R_{\odot}$. The gravitational and ionization energy are 5.6$\times 10^{14}$ erg g^{-1} and 1.9–2.1$\times 10^{13}$ erg g^{-1}, respectively. In cases where the model does not satisfy the constraints from the observations, these are marked as [a-e] (details in Table 4). The H2 model could not satisfy all the constraints together for several blobs because the lines Lyα, C III, C II, N III might come from different regions along the line of sight. For all the acceptable models, the heating energy for H1 is higher by nearly one order of magnitude than that for H2, and it exceeds the kinetic energy. A recent study of heating rates for ICME from *Helios 1* and *Helios 2* observations found that plasma turbulence heats the protons and alpha particles and determined the heating rates to be 1.9 $\times 10^{8}$ erg g^{-1} s^{-1} at 0.3 AU and 1.9 $\times 10^{5}$ erg g^{-1} s^{-1} at 20 AU (Liu et al. 2006). The heating rate, 1$\times 10^{11}$ erg g^{-1} s^{-1} at 0.01 AU, estimated by extrapolating from their study (Figure 6 in their paper) is similar to our result of the heating rate, 5$\times 10^{-7}$ erg cm^{-3} s^{-1} at 2.4 $R_{\odot}$ (taking the electron density 1.0 $\times$ 10^{6} cm^{-3} and the mass from assuming 10% helium, 1.974$\times 10^{-24}$ g).

The heating energies from the Kumar & Rust (1996) model are also greater than the kinetic energy. For all acceptable models, 70–90% of the magnetic energy goes into the heating energy, in agreement with their theoretical calculation. The 2001 December 13 event is probably a prominence eruption and it is presumably defined by the magnetic field (see Figure 2). The fractions of the magnetic energy that go into heat for the earlier observed blobs are higher than these later ones. For H2, we could not find a heating rate that satisfies the intensities of those low-temperature lines. It is possible that the CME plasma inside the flux rope does not follow the heating law of the Kumar & Rust magnetic cloud model or that the assumed self-similar expansion is not a good approximation in the early stages of the eruption.

Figure 16 shows the timescale of radiative cooling, adiabatic cooling, and thermal conduction for one of the acceptable models for H1 of C.5 ($Q \propto n$). We can use the temperature gradients from this model with the *Spitzer* thermal conductivity to evaluate the importance of the thermal conduction contribution to the heating. Larger temperature gradients would give too low a temperature at the height of the UVCS slit, so this gives an upper limit to the thermal conduction contribution. Other parameterizations of the heating rate could differ slightly, but not at the level needed for thermal conduction to balance adiabatic cooling. The thermal conductive flux and timescale can be estimated as

$$\nabla F_c = -\kappa_0 \left[\left(\frac{T_i + T_{i-1}}{2} \right)^{5/2} \frac{(T_i - T_{i-1})}{(l_i - l_{i-1})} - \left(\frac{T_{i+1} + T_i}{2} \right)^{5/2} \times \frac{(T_{i+1} - T_i)}{(l_{i+1} - l_i)} \right] / (l_{i+1} - l_{i-1}) \quad (9)$$

and

$$\tau_i = \frac{\frac{5}{2} n_{i-1} k T_{i-1}}{\nabla F_c}, \quad (10)$$

respectively. Here i is the time step and ∇F_c is the divergence of the conductive flux, κ_0 is $1.8 \times 10^{-5}/\ln \Lambda$ erg cm^{-1} K$^{-7/2}$ s^{-1}, and $\ln \Lambda$ is the Coulomb logarithm. In the earliest stage of the expansion, the timescale of thermal conduction is much smaller than other cooling timescales. In this stage, the thermal conduction would maintain the initial high temperature and might change the temperature structure during the first 200 s and flatten out the initial steep drop (or rise) in temperature if the temperature gradient lies along the magnetic field. In the plot of the thermal conduction time scale, the peak around 300 s is due to the change of the sign of the divergence of the conductive flux. Those plots indicate that the adiabatic cooling is much more important than other terms after earlier stages. We have assumed classical *Spitzer* conductivity in Equation (9). Saturated conductivity would provide a smaller heating rate, but it is possible that a non-Maxwellian velocity distribution gives a larger conductive heating rate.

Due to the expansion of CME, the plasma cools rapidly at earlier stages, and then the heating energy becomes the major contribution in the energy budget of the ejected CME plasma, even greater than the kinetic energy. Guhathakurta et al. (2006) studied the heating of the corona and they also found that the thermal and non-thermal heating terms contribute to the temperature and heat flux in the low corona (see Figure 4 in their paper). A similar result for the heating energy of CME plasma based on the *Advanced Composition Explorer* (*ACE*) observations shows that the plasma requires further heating following filament eruption (Rakowski et al. 2007).

Our results confirm the studies of Akmal et al. (2001) for a different event and obtain a narrower range of the heating rates in both ions and electrons. Also our study shows that heating rates are consistent with Kumar & Rust's (1996) model. About 75% of the magnetic energy goes into the heating energy for the O VI observation with Kumar & Rust's model, in agreement with their prediction.

7. SUMMARY

UVCS observed Doppler-shifted material in the O VI 1032 Å, Lyα 1216 Å, and C III 977 Å lines on 2001 December 13. Fainter spectral lines, O V] 1218.35 Å, [O V] 1213.9 Å, N III 991.58 Å, and C II 1037.02 Å, were observed in several exposures. A three-dimensional reconstruction of the 2001 December 13 partial halo CME has been made based on the O VI, Lyα, and C III lines. The reconstructed structure shows the distribution of those ions as viewed from all directions. The structure viewed from the backside of the Sun toward the Earth looks like a hollow flux rope. The C III emission is located in the innermost part of the ejected CME material. The reconstructed structure is also used to find the column density with LASCO observations. We investigate the heating rates by a procedure similar to that of Akmal et al. (2001). For the individual knots observed by UVCS, we generate a large grid of models having different initial conditions and forms of the heating function. We find that continuous heating is required to match the UVCS observations. The temperature evolution shows a rapid decrease at lower heights and earlier stages, and then heating is required to increase the temperature to match the observations. To match the O VI bright knots, a higher heating rate is required such that the heating energy is greater than the kinetic energy. The temperatures for the O VI and Lyα, C III, C II, and N III emission indicate that different heating rates are required for the bright knots in those lines. About 75% of the magnetic energy goes into the heating energy for the O VI observation with Kumar & Rust's (1996) model, in agreement with their prediction, but those models do not match the cool line blobs.

We thank G.-S. Choe and Y.-J. Moon for helpful discussion on this paper. This work was supported by the Korea Research Foundation (ABRL-R14-2002-043-01001-0) and Grant NNG06GG78G to the Smithsonian Astrophysical Observatory. J.-Y. Lee acknowledges the support of the Korea Research Foundation (KRF-2005-070-C000059), the Astrophysical Research Center for the Structure and Evolution of the Cosmos (ARC-SEC) of Korea Science and Engineering Foundation through the Science Research Center (SRC) program, and Grant NNM07AA02C to the Smithsonian Astrophysical Observatory.

REFERENCES

Akmal, A., Raymond, J. C., Vourlidas, A., Thompson, B., Ciaravella, A., Ko, Y.-K., Uzzo, M., & Wu, R. 2001, ApJ, 553, 922
Allen, L. A., Habbal, S. R., & Hu, Y. Q. 1998, J. Geophys. Res., 103, 6551
Burkepile, J. T., Hundhausen, A. J., Stanger, A. L., St. Cyr, O. C., & Seiden, J. A. 2004, J. Geophys. Res., 109, A03103
Chen, J., Marqué, C., Vourlidas, A., Krall, J., & Schuck, P. W. 2006, ApJ, 649, 452
Ciaravella, A., Raymond, J. C., & Kahler, S. W. 2006, ApJ, 652, 774
Ciaravella, A., Raymond, J. C., Reale, F., Strachan, L., & Peres, G. 2001, ApJ, 557, 351
Ciaravella, A., Raymond, J. C., van Ballegooijen, A., Starchan, L., Vourlidas, A., Li, J., Chen, J., & Panasyuk, A. 2003, ApJ, 597, 1118
Crifo, F., Picat, J. P., & Cailloux, M. 1983, Sol. Phys., 83, 143

Dere, K. P., Landi, E., Mason, H. E., Monsignori-Fossi, B. F., & Young, P. R. 1997, A&AS, 125, 149
Dere, K. P., Wang, D., & Howard, R. 2006, ApJ, 620, 119
Emslie, et al. 2004, J. Geophys. Res., 109, A10104
Emslie, A. G., Dennis, B. R., Holman, G. D., & Hudson, H. S. 2005, J. Geophys. Res., 110, A11103
Fisher, R. R., & Munro, R. H. 1984, ApJ, 280, 428
Filippov, B., & Koutchmy, S. 2002, Sol. Phys., 208, 283
Guhathakurta, M., Sittler, E. C., Jr., & Ofman, L. 2006, J. Geophys. Res., 111, A11215
Grevesse, N., & Sauval, A. J. 1998, Space Sci. Rev., 85, 161
Howard, T. A., Fry, C. D., Johnston, J. C., & Webb, D. F. 2007, ApJ, 667, 610
Kaiser, M. L. 2005, Adv. Space Res., 36, 1483
Ko, Y.-K., Raymond, J. C., Zurbuchen, T. H., Riley, P., Raines, J. M., & Strachan, L. 2006, ApJ, 646, 1275
Kohl, J. L., et al. 1995, Sol. Phys., 162, 313
Kohl, J. L., et al. 1997, Sol. Phys., 175, 613
Krall, J. 2007, ApJ, 657, 559
Krall, J., & St. Cyr, O. C. 2006, ApJ, 652, 1740
Kumar, A., & Rust, D. M. 1996, J. Geophys. Res., 101, 15667
Landi, E., Del Zanna, G., Young, P. R., Dere, K. P., Mason, H. E., & Landini, M. 2006, ApJS, 162, 261
Lee, J.-Y., Raymond, J. C., Ko, Y.-K., & Kim, K.-S. 2006, ApJ, 651, 566
Liu, Y., Richardson, J. D., Belcher, J. W., & Kasper, J. C. 2006, J. Geophys. Res., 111, A01102
Lynch, B. J., Antiochos, S. K., DeVore, C. R., Luhmann, J. G., & Zurbuchen, T. H. 2008, ApJ, 683, 1192
Lynch, B. J., Antiochos, S. K., MacNiece, P. J., Zurbuchen, T. H., & Fisk, L. A. 2004, ApJ, 617, 589
Lynch, B. J., Gruesbeck, J. R., Zurbuchen, T. H., & Antiochos, S. K. 2005, J. Geophys. Res., 110, A08107
Michalek, G., Gopalswamy, N., & Yashiro, S. 2003, ApJ, 584, 472
Moran, T. G., & Davila, J. M. 2004, Science, 305, 66
Rakowski, C. E., Laming, J. M., & Lepri, S. T. 2007, ApJ, 667, 602
Raymond, J. C. 1979, ApJS, 39, 1
Raymond, J. C. 2002, in Proc. SOHO 11 Symp., From solar Min to Max : Half a Solar Cycle with SOHO, ed. A. Wilson (ESA SP-508; Noordwijk: ESA) 421
Shiota, D., Isobe, H., Chen, P. F., Yamamoto, T., Sakajiri, T., & Shibata, K. 2005, ApJ, 634, 663
Subramanian, P., & Vourlidas, A. 2007, A&A, 467, 685
Uralov, A. M., Grechnev, V. V., & Hudson, H. S. 2005, J. Geophys. Res., 110, A05104
Vourlidas, A., Subramanian, P., Dere, K. P., & Howard, R. A. 2000, ApJ, 534, 456
Xue, X. H., Wang, C. B., & Dou, X. K. 2006, J. Geophys. Res., 110, A08103
Yeh, C.-T., Ding, M. D., & Chen, P. F. 2005, Sol. Phys., 229, 313
Zhao, X. P., Plunkett, S. P., & Liu, W. 2002, J. Geophys. Res., 107(A8), 1223
Zie, H., Ofman, L., & Lawrence, G. 2004, J. Geophys. Res., 109, A03109